

Nonlinear Anisotropy in Phase-Tuned Wide-Gap Halides

L. Landivar Scott,¹ L. M. Vogl,² C. Klenke,³ S. Puri,¹ and H. Nakamura^{1,3,*}

¹*Department of Physics, University of Arkansas, AR 72701, USA*

²*Max Planck Institute for Sustainable Materials, 40237 Düsseldorf, Germany*

³*Department of Materials Science and Engineering, University of Arkansas, AR 72701, USA*

Silver iodide (AgI) thin films offer a compelling platform for studying nonlinear optical phenomena due to their intrinsic noncentrosymmetric lattice and direct band gap. Here, we investigate the nonlinear optical properties of AgI thin films grown by physical vapor deposition that selectively produce zincblende (γ -AgI) and wurtzite (β -AgI) phases. Using a combination of polarization-resolved second harmonic generation (SHG) and two-photon photoluminescence (2PPL) spectroscopy, we identify clear phase- and morphology-dependent anisotropic nonlinear responses. Triangular γ -AgI(111) flakes exhibit sixfold SHG symmetry and isotropic 2PPL emission, while rod-shaped β -AgI(101) samples display twofold-symmetric patterns in both SHG and 2PPL, which are explained by polarization analysis using second- and third- order nonlinear susceptibilities. These findings establish AgI as a promising halide semiconductor platform for phase-selective nonlinear optics and quantum photonic applications.

I. INTRODUCTION

Nonlinear optical effects in crystalline materials provide powerful means of probing symmetry, band structure, and light-matter interactions. In particular, second harmonic generation (SHG) and two-photon photoluminescence (2PPL) have become indispensable tools for studying noncentrosymmetric materials and their symmetry-dependent responses [1]. In two-dimensional (2D) materials such as transition-metal dichalcogenides (TMDs) and hexagonal boron nitride, interlayer stacking and rotational alignment can reversibly break or restore inversion symmetry, thereby modulating the nonlinear optical response [2–4]. Such stacking-dependent SHG effects demonstrate that structural symmetry control at the atomic scale provides a robust handle for engineering nonlinearities in low-dimensional systems.

Beyond van der Waals semiconductors, halide compounds are emerging as a promising new class of nonlinear materials [5–7]. Their large polarizability, tunable electronic structure, and propensity to form noncentrosymmetric lattices give rise to strong $\chi^{(2)}$ and $\chi^{(3)}$ responses even in bulk phases. Lead halide perovskites and copper or silver halides have exhibited tunable second- and third-order nonlinearities due to structural phase transitions, excitonic resonances, and strain [8–11]. However, our understanding of the correlation between crystalline phase and nonlinear response in simple binary halides has been underdeveloped. Silver iodide (AgI) is particularly intriguing because it exhibits polymorphism between zincblende (γ -AgI) and wurtzite (β -AgI) phases at ambient conditions [12–14] - both being direct-gap, noncentrosymmetric semiconductors [15]. This makes AgI a rare system for isolating phase-induced effects on nonlinear optical processes within the same chemical composition.

In this Letter, we investigate phase-dependent nonlinear optical effects in silver iodide thin films synthesized by controlled physical vapor deposition. Using polarization-resolved SHG and two-photon photoluminescence spectroscopy, we reveal

distinct anisotropic responses associated with the γ -AgI(111) and β -AgI(101) phases. The results demonstrate how crystallographic phase dictate nonlinear light–matter interactions in halide semiconductors, offering a pathway toward phase-engineered halide platforms for nanoscale optoelectronic and quantum photonic applications.

II. GROWTH AND STRUCTURAL CHARACTERIZATION

Silver iodide (AgI) thin films were grown using physical vapor deposition (PVD) from commercially available, high-purity AgI powder. The source powder was placed at the center of the furnace, while silicon substrates with a 90 nm-thick SiO_2 layer were mounted on a separate alumina boat positioned downstream. After vacuum pumping for approximately five minutes, a gas mixture of 96 % argon (Ar) and 4 % H_2 was introduced in the reverse (substrate-to-powder) direction. Growth was carried out at 450 °C for samples yielding predominantly triangular and hexagonal morphologies, and at 470 °C for samples exhibiting rod-like structures. In all cases, the growth was quenched by sliding both powder and substrates away from the hot zone of the furnace.

High-resolution scanning transmission electron microscopy (HRSTEM) was used to determine the AgI phases (Fig. 1); complementary evidence, including XRD, is provided in the Supplementary Information. A lattice-spacing analysis and zone-axis calculations identify low-temperature crystals as consistent with the zincblende γ -AgI(111) [Fig. 1(e)], whereas the higher-temperature crystals exhibit spacings and orthogonal-plane relationships consistent with β -AgI(101) plane as the exposed surface (see Supplementary Information). These assignments are further supported by polarization-resolved SHG and 2PPL analyses (see below). The combined STEM and optical signatures therefore suggest that triangular platelets preferentially adopt the zincblende γ -AgI, while elongated rods are associated with the hexagonal wurtzite β -AgI.

* hnakamur@uark.edu

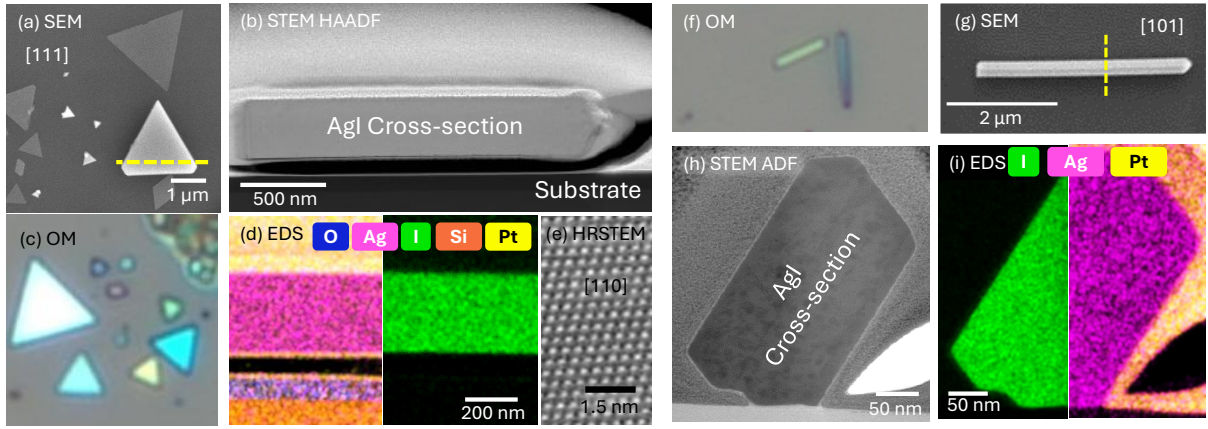


FIG. 1. Electron microscopy and spectroscopy characterization of two AgI morphologies prepared as FIB lift-out cross-section lamellae. Triangular platelet: (a) SEM plan-view image of triangular platelets, with a dashed yellow line indicating the cut location for cross-sectioning. (b) HAADF-STEM cross-section reveals a uniform AgI film of approximately 500 nm thickness on a Si substrate. (c) Bright-field optical image of the same sample confirms the characteristic triangular morphology. (d) STEM-EDS mapping shows a stoichiometric and compositionally uniform distribution of Ag (magenta) and I (green); O (blue), Si (red), and Pt (yellow) originate from the substrate and protective cap, respectively. (e) High-resolution STEM image along a zone axis reveals atomic lattice fringes consistent with the γ -AgI(111) stacking sequence with a zone axis [110]. Rod-like platelet: (f) Optical micrograph of an elongated nanorod grown at higher temperature. (g) SEM plan-view of a nanorod, with the yellow dashed line indicating the cross-section cut for TEM. (h) ADF-STEM cross-section shows a compact, rectangular shape with dense internal microstructure. (i) STEM-EDS elemental mapping confirms the rod is composed of Ag and I, with a stoichiometric distribution.

III. RESULTS AND DISCUSSION

Phase-selective SHG and excitonic 2PPL

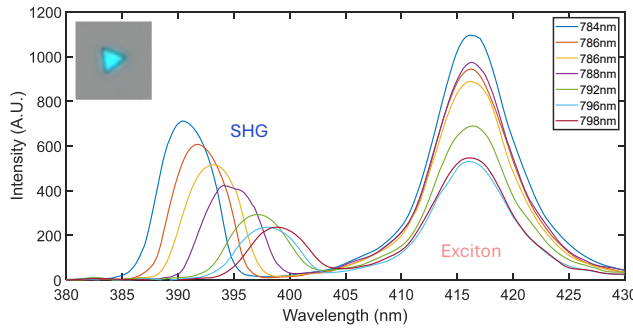


FIG. 2. Wavelength-resolved nonlinear emission from an individual AgI triangular flake. Normalized photoluminescence spectra were collected while tuning the excitation wavelength from 784 nm to 798 nm. Each trace exhibits two distinct features: (i) a narrow band at 388–398 nm attributed to second-harmonic generation (SHG), which shifts according to $\lambda/2$ of the fundamental excitation; and (ii) a broader band centered at 412–420 nm assigned to excitonic emission, whose peak position remains nearly constant while its intensity varies with the pump wavelength. The inset shows a representative triangular crystal from the same substrate used for the measurement. All intensities are plotted in arbitrary units (A.U.).

SHG and 2PPL measurements were performed using a custom system described in Ref.[16]. An ultrafast pulsed laser with a pulse width of 80 fs and a near-infrared wavelength of 780 – 830 nm was used as an incident beam. In polarization-

resolved measurements, the laser beam passed through a linear polarizer before reaching the sample and another polarizer selected polarization component parallel to the incident laser polarization in the detection path, while sample being rotated by a rotational stage. All the optical measurements were performed at room temperature.

Figure 2 presents wavelength-resolved nonlinear emission spectra from an individual AgI triangular flake. The spectra reveal two distinct peaks: (i) a shorter-wavelength band at 388–398 nm corresponding to SHG, confirmed by its $\lambda_{out} = \lambda_{in}/2$ dependence and (ii) a broader peak at approximately 416 nm, assigned to the excitonic transition. The exciton emission varied from 412 nm to 440 nm depending on the measured flake, likely originating from different crystal phases as detailed below. Since the fundamental laser energy is less than the estimated bandgap of around 3 eV in AgI [8], the observed exciton peak is attributed to 2PPL.

To study phase-dependent nonlinear anisotropy in AgI, we have performed polarization-resolved SHG and 2PPL measurements for samples with different morphologies: triangular platelets and rod-shaped AgI. Distinct angular anisotropy was observed in SHG from those crystals, exhibiting a sixfold “flower” pattern for the triangular AgI (Fig.3(b)) compared to a twofold “butterfly” pattern for the AgI rod (Fig.3(e)). The 2PPL also showed distinct behavior depending on the morphologies: We observe isotropic circular response for the triangular island (Fig.3(c)) while twofold uniaxial pattern in the rod (Fig.3(f)). Note that although triangular AgI consistently showed consistent angular-SHG patterns, the patterns derived from rod-shaped AgI sometimes indicated the impact of beam damage (see Supplementary Materials).

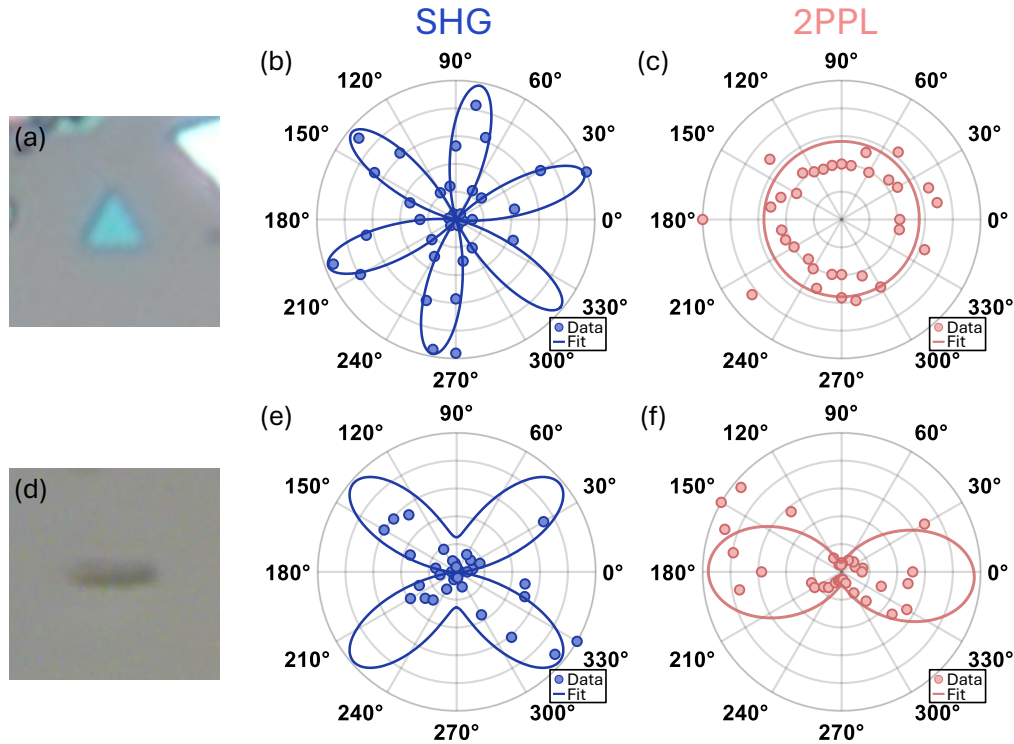


FIG. 3. Polarization-resolved nonlinear-optical response of two AgI micro-crystals. (a) Optical micrograph of a triangular flake; (b) SHG polar plot from flake (a), exhibiting six-lobed pattern that follows a $\cos^2[3(\theta - \phi_0)]$ dependence; (c) 2PPL response of the triangle. (d) Optical micrograph of a nanorod; (e) SHG polar plot recorded from the nanorod showing twofold symmetry aligning with simulation values for $d_1 > d_2$; (f) corresponding 2PPL revealing pronounced anisotropy, contrasting the isotropic response from (a) – maxima are aligned with the long axis of the rod.

Analysis of SHG and 2PPL Angular Dependence

To analyze the nonlinear anisotropy observed in zincblende and wurtzite phases of AgI with distinct morphologies, we employ second- and third-order nonlinear optical formalisms that account for both crystal symmetry and the experimental geometry.

Second-harmonic generation (SHG). The three orthogonal components of the second-order nonlinear polarization $P_{i,2\omega}$ are expressed as

$$P_{i,2\omega} = 2\epsilon_0 \sum_{j,k} d_{ijk}^{(2)}(2\omega; \omega, \omega) E_j E_k, \quad (1)$$

where ϵ_0 is the permittivity of free space, $d_{ijk}^{(2)} = \frac{1}{2} \chi_{ijk}^{(2)}$ is the second-order susceptibility tensor, and $E_j E_k$ are components of the fundamental electric field.

For the zincblende phase of AgI (point group $4\bar{3}m$), the nonvanishing elements of d_{ijk} are [1] $d_{xyz} = d_{yzx} = d_{zxy} \equiv d_{14}$, assuming $d_{ijk} = d_{ikj}$ symmetry:

$$\mathbf{d}_{zb} = \begin{bmatrix} 0 & 0 & 0 & d_{14} & 0 & 0 \\ 0 & 0 & 0 & 0 & d_{14} & 0 \\ 0 & 0 & 0 & 0 & 0 & d_{14} \end{bmatrix}. \quad (2)$$

For the wurtzite phase (point group $6mm$), the nonvanishing elements are $d_{zxx} = d_{zyy} = d_{yyz} = d_{xxz} \equiv d_{15}$ and $d_{zzz} \equiv$

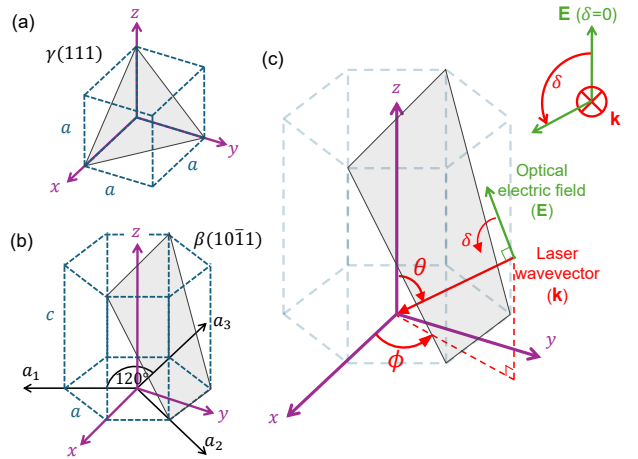


FIG. 4. Relation between Cartesian and crystallographic coordinate systems, and definition of beam orientation angles. (a) Alignment of Cartesian and crystallographic axes in a cubic unit cell. (b) Alignment of Cartesian and crystallographic axes in a hexagonal unit cell. (c) Definition of the angles θ , ϕ , and δ describing the orientation of the incident laser beam (wave vector \mathbf{k}) and its optical electric field \mathbf{E} .

d_{33} [1]:

$$\mathbf{d}_{wz} = \begin{bmatrix} 0 & 0 & 0 & 0 & d_{15} & 0 \\ 0 & 0 & 0 & d_{15} & 0 & 0 \\ d_{15} & d_{15} & d_{33} & 0 & 0 & 0 \end{bmatrix}. \quad (3)$$

The x , y , and z labels correspond to laboratory axes aligned with the crystallographic axes as defined in Fig. 4.

To analyze polarization-resolved SHG when \mathbf{E} is rotated within a crystallographic plane, we introduce an effective scalar susceptibility

$$d_{\text{eff}}(\theta, \phi, \delta) = (e_{3x}, e_{3y}, e_{3z}) \cdot \mathbf{d} \begin{bmatrix} e_{1x}^2 \\ e_{1y}^2 \\ e_{1z}^2 \\ 2e_{1y}e_{1z} \\ 2e_{1x}e_{1z} \\ 2e_{1x}e_{1y} \end{bmatrix}, \quad (4)$$

where e_3 denotes the SH polarization direction after the analyzer, and e_1 is the polarization of the fundamental beam. In our configuration $e_3 = e_1 = e$, described by

$$\begin{aligned} e_x &= \sin \phi \sin \delta - \cos \theta \cos \phi \cos \delta, \\ e_y &= -\cos \phi \sin \delta - \cos \theta \sin \phi \cos \delta, \\ e_z &= \sin \theta \cos \delta. \end{aligned} \quad (5)$$

Rotation of polarization within the zincblende (111) plane corresponds to rotating δ from 0° to 360° at fixed $\theta = 54.74^\circ$, $\phi = 45^\circ$, while for wurtzite (101) $\theta = 62^\circ$ and $\phi = 30^\circ$. The scalar quantity $d_{\text{eff}}(\theta, \phi, \delta)$ can thus be computed and scaled to fit the SHG angular pattern.

Two-photon absorption (2PA) and two-photon photoluminescence (2PPL). The measured 2PPL intensity is assumed proportional to the absorbed two-photon energy and unpolarized emission due to inelastic scattering prior to emission, giving $I_{\text{2PPL}}(\theta, \phi, \delta) \propto I_{\text{2PA}}(\theta, \phi, \delta)$. The two-photon absorption (2PA) process originates from the imaginary part of the third-order nonlinear susceptibility, $\chi^{(3)}$, which governs the third-order polarization [1]

$$P_i^{(3)}(\omega) = \varepsilon_0 \chi_{ijkl}^{(3)}(\omega; \omega, \omega, -\omega) E_j E_k E_l^*. \quad (6)$$

The time-averaged absorbed power density is [17]

$$\langle \dot{W}_3 \rangle = \left\langle \mathbf{E} \cdot \frac{d\mathbf{P}^{(3)}}{dt} \right\rangle = \frac{\omega \varepsilon_0}{2} \text{Im} \left[\chi_{ijkl}^{(3)} \right] E_i^* E_j E_k E_l^*. \quad (7)$$

This E^4 scaling is consistent with quantum mechanical perturbation theory calculations [18, 19] and macroscopic susceptibility analyses [20, 21].

To analyze the angular dependence of this scalar quantity proportional to $E_i^* E_j E_k E_l^*$, we first note that in our case of degenerate 2PA with the same linear polarization, the two absorbed photons are indistinguishable, allowing us to rearrange the quartic term into a pair of quadratic electric field products, $E_i^* E_j^*$ and $E_k E_l$. We therefore group the quadratic field products into a six-component vector,

$$v(\delta) = [E_x^2 \ E_y^2 \ E_z^2 \ 2E_y E_z \ 2E_z E_x \ 2E_x E_y]^\top, \quad (8)$$

so that the 2PA signal may be written compactly as a quadratic form

$$I_{\text{2PA}}(\theta, \phi, \delta) \propto v(\delta)^\top B v(\delta). \quad (9)$$

Here, B is a real, symmetric 6×6 matrix that encapsulates all crystal-symmetry constraints and fully determines the angular dependence of 2PA through the direction cosines $(E_x, E_y, E_z) = (e_x, e_y, e_z)$ in Eq. (5). This is the same structure that underlies Voigt contraction for other fourth-rank optical tensors (e.g., Kerr and elastic tensors [22, 23]), and although not frequently used in the context of 2PA, it makes crystal-symmetry constraints (cubic vs. hexagonal) transparent. Angular anisotropy of 2PA under more general conditions is discussed, for example, in Refs. [20, 21, 24].

Expanding Eq. (9) gives

$$\begin{aligned} I_{\text{2PA}} &\propto B_{11} E_x^4 + B_{22} E_y^4 + B_{33} E_z^4 \\ &\quad + 2(B_{12} E_x^2 E_y^2 + B_{13} E_x^2 E_z^2 + B_{23} E_y^2 E_z^2) \\ &\quad + B_{44} (2E_y E_z)^2 + B_{55} (2E_z E_x)^2 + B_{66} (2E_x E_y)^2. \end{aligned} \quad (10)$$

Zincblende ($4\bar{3}m$) form of B . For cubic (zincblende) symmetry, the tensor simplifies to

$$B_{zb} = \begin{bmatrix} B_{11} & B_{12} & B_{12} & 0 & 0 & 0 \\ B_{12} & B_{11} & B_{12} & 0 & 0 & 0 \\ B_{12} & B_{12} & B_{11} & 0 & 0 & 0 \\ 0 & 0 & 0 & B_{44} & 0 & 0 \\ 0 & 0 & 0 & 0 & B_{44} & 0 \\ 0 & 0 & 0 & 0 & 0 & B_{44} \end{bmatrix}, \quad (11)$$

a form commonly used for cubic semiconductors exhibiting zincblende-type symmetry [22, 23].

Wurtzite (6mm) form of B . For crystals with 6mm symmetry, shear planes containing the c -axis are equivalent, giving [22, 23]

$$B_{wz} = \begin{bmatrix} B_{11} & B_{12} & B_{13} & 0 & 0 & 0 \\ B_{12} & B_{11} & B_{13} & 0 & 0 & 0 \\ B_{13} & B_{13} & B_{33} & 0 & 0 & 0 \\ 0 & 0 & 0 & B_{44} & 0 & 0 \\ 0 & 0 & 0 & 0 & B_{44} & 0 \\ 0 & 0 & 0 & 0 & 0 & B_{66} \end{bmatrix}. \quad (12)$$

Following the group-theoretical discussions of Inoue and Toyozawa [18] for two-photon absorption in semiconductors, the fourth-rank susceptibility entering the 2PPL process can be decomposed into a small number of scalar invariants fixed by crystal symmetry. For zincblende, the two-photon absorption tensor can be written as a sum of only two linearly independent invariants: one isotropic term and one cubic-anisotropy term.

$$\beta_1^{(zb)} = B_{11} + 2B_{12}, \quad \beta_2^{(zb)} = B_{11} - (B_{11} + 2B_{12}) \quad (13)$$

where $\beta_1^{(zb)}$ sets the isotropic background, while $\beta_2^{(zb)}$ controls the cubic anisotropy. In contrast, the lower hexagonal symmetry of wurtzite allows four independent invariants in the same decomposition. The corresponding 2PPL intensity then

depends on four independent scalar coefficients, which are distinct linear combinations of the underlying tensor elements.

$$\begin{aligned}\beta_1^{(wz)} &= B_{33}, & \beta_2^{(wz)} &= 2B_{13} + 4B_{44}, \\ \beta_3^{(wz)} &= B_{11}, & \beta_4^{(wz)} &= 2B_{12} + 4B_{66} - 6B_{11}\end{aligned}\quad (14)$$

where $\beta_3^{(wz)}$ governs the in-plane isotropic part and $\beta_4^{(wz)}$ the in-plane uniaxial (twofold) anisotropy, whereas $\beta_1^{(wz)}$ and $\beta_2^{(wz)}$ weight the out-of-plane and mixed (E_z) contributions.

The results of theoretical fits to SHG and 2PPL are shown as solid lines in Fig. 3. The parameters used for the fits are summarized in the Supplementary Material. For zincblende(111), the theory fits SHG flower pattern well, and the nearly circular 2PPL is reproduced with $|\beta_2^{(zb)}| \ll |\beta_1^{(zb)}|$. This is consistent with earlier results on GaAs(111) [20]. The butterfly-shaped SHG for rod-shaped AgI is also reproduced by the theory assuming wurtzite (101) for its top surface. For 2PPL, fits to the rod data require $|\beta_4^{(wz)}| > |\beta_3^{(wz)}|$ with a finite $\beta_2^{(wz)}$ to reproduce the observed twofold pattern and its axis.

IV. SUMMARY

In conclusion, we have investigated the nonlinear optical properties of silver iodide (AgI) thin films using polarization-resolved second harmonic generation and two-photon photoluminescence spectroscopy. By tuning the physical vapor deposition (PVD) conditions, we selectively grew zincblende (γ -AgI) and wurtzite (β -AgI) phases. Our measurements reveal that triangular γ -AgI(111) flakes exhibit sixfold SHG symmetry and isotropic 2PPL emission, while rod-like β -AgI(101) crystals display a butterfly-shaped SHG response with twofold-symmetric 2PPL. These contrasting angular anisotropies are consistent with theoretical analysis and underscore the role of crystal phase dictating nonlinear optical behavior. The ability to engineer the phase and resultant morphology of AgI provides a promising platform for tailoring optical anisotropy and nonlinear light-matter interactions at the nanoscale.

ACKNOWLEDGMENTS

We thank N. Nagaosa for helpful discussions. The work is supported by the Office of the Secretary of Defense for Research and Engineering under Award No. FA9550-23-1-0500 and the MonArk NSF Quantum Foundry from the National Science Foundation under Award No. DMR-1906383. L. L. S. was supported by the University of Arkansas Honors College Research Grant and the Chan and Chen Endowed Research Scholarship.

[1] R. W. Boyd, *Nonlinear Optics*, 4th ed. (Academic Press, 2020).

[2] K. F. Mak, C. Lee, J. Hone, J. Shan, and T. F. Heinz, Atomically thin MoS₂: a new direct-gap semiconductor, *Physical review letters* **105**, 136805 (2010).

[3] Y. Li, Y. Rao, K. F. Mak, Y. You, S. Wang, C. R. Dean, and T. F. Heinz, Probing symmetry properties of few-layer MoS₂ and h-BN by optical second-harmonic generation, *Nano letters* **13**, 3329 (2013).

[4] K. L. Seyler, J. R. Schaibley, P. Gong, P. Rivera, A. M. Jones, S. Wu, J. Yan, D. G. Mandrus, W. Yao, and X. Xu, Electrical control of second-harmonic generation in a WSe₂ monolayer transistor, *Nature nanotechnology* **10**, 407 (2015).

[5] F. Saouma, C. Stoumpos, J. Wong, M. Kanatzidis, and J. Jang, Selective enhancement of optical nonlinearity in two-dimensional organic-inorganic lead iodide perovskites, *Nature communications* **8**, 742 (2017).

[6] G. Yumoto, F. Harata, T. Nakamura, A. Wakamiya, and Y. Kanemitsu, Electrically switchable chiral nonlinear optics in an achiral ferroelectric 2D van der waals halide perovskite, *Science Advances* **10**, eadq5521 (2024).

[7] J. Xu, X. Li, J. Xiong, C. Yuan, S. Semin, T. Rasing, and X.-H. Bu, Halide perovskites for nonlinear optics, *Advanced Materials* **32**, 1806736 (2020).

[8] A. Goldmann, Band structure and optical properties of tetrahedrally coordinated Cu-and Ag-halides, *physica status solidi (b)* **81**, 9 (1977).

[9] R. Dinges, D. Fröhlich, and C. Uihlein, Two-photon absorption of anisotropic excitons in β -AgI, *physica status solidi (b)* **76**, 613 (1976).

[10] A. Alexander, M. Gupta, D. Kottilil, B. B. Rath, J. J. Vittal, and W. Ji, Anisotropic two-photon absorption and second harmonic generation in single crystals of silver (i) coordination complexes, *ACS Applied Materials & Interfaces* **13**, 31891 (2021).

[11] M. Nakamura, Y.-H. Chan, T. Yasunami, Y.-S. Huang, G.-Y. Guo, Y. Hu, N. Ogawa, Y. Chiew, X. Yu, T. Morimoto, *et al.*, Strongly enhanced shift current at exciton resonances in a non-centrosymmetric wide-gap semiconductor, *Nature Communications* **15**, 9672 (2024).

[12] G. Burley, Polymorphism of silver iodide, *American Mineralogist: Journal of Earth and Planetary Materials* **48**, 1266 (1963).

[13] J. Patnaik and C. Sunandana, Studies on gamma silver iodide, *Journal of Physics and Chemistry of Solids* **59**, 1059 (1998).

[14] F. Sabath, C. Aleff, A. Latus, R. Bechstein, and A. Kühnle, Atomic-resolution imaging of the ice nucleating silver iodide surface: Does this polar surface reconstruct at the atomic scale?, *Advanced Materials Interfaces* **9**, 2201065 (2022).

[15] A. Laref, W. Sekkal, A. Zaoui, M. Certier, and H. Aourag, Tight-binding calculations of electronic properties of AgI, *Journal of applied physics* **86**, 4435 (1999).

[16] S. Puri, S. Patel, J. L. Cabellos, L. E. Rosas-Hernandez, K. Reynolds, H. O. Churchill, S. Barraza-Lopez, B. S. Menzoza, and H. Nakamura, Substrate interference and strain in the second-harmonic generation from MoSe₂ monolayers, *Nano*

Letters **24**, 13061 (2024).

- [17] L. D. Landau and E. M. Lifshitz, *Electrodynamics of Continuous Media*, Vol. 8 (Pergamon Press, 1984).
- [18] M. Inoue and Y. Toyozawa, Two-photon absorption and energy band structure, Journal of the Physical Society of Japan **20**, 363 (1965).
- [19] M. A. C. Nascimento, The polarization dependence of two-photon absorption rates for randomly oriented molecules, Chemical Physics **74**, 51 (1983).
- [20] M. D. Dvorak, W. A. Schroeder, D. R. Andersen, A. L. Smirl, and B. S. Wherrett, Measurement of the anisotropy of two-photon absorption coefficients in zincblende semiconductors, IEEE Journal of Quantum Electronics **30**, 256 (1994).
- [21] D. C. Hutchings, Theory of the polarization dependence of two-photon absorption, Journal of Modern Optics **41**, 2309 (1994).
- [22] J. F. Nye, *Physical Properties of Crystals: Their Representation by Tensors and Matrices* (Oxford University Press, 1985).
- [23] A. Yariv and P. Yeh, *Optical Waves in Crystals: Propagation and Control of Laser Radiation* (Wiley, 1984).
- [24] L. Krauss-Kodytek, W.-R. Hannes, T. Meier, C. Ruppert, and M. Betz, Nondegenerate two-photon absorption in ZnSe: experiment and theory, Physical Review B **104**, 085201 (2021).

Supporting Information for:

Nonlinear Anisotropy in Phase-Tuned Wide-Gap Halides

L. Landivar Scott¹, L. M. Vogl², C. Klenke³, S. Puri¹, and H. Nakamura^{1,3}

¹ Department of Physics, University of Arkansas, AR 72701, USA

² Max Planck Institute for Sustainable Materials, 40237 Düsseldorf, Germany

³ Department of Materials Science and Engineering, University of Arkansas, AR 72701, USA

Corresponding author: hnakamur@uark.edu

Table of Contents

1. Transmission Electron Microscopy Analysis
2. Polarization-Resolved SHG and 2PPL Summary
3. SHG Simulation Values
4. 2PPL Simulation Values

1. TRANSMISSION ELECTRON MICROSCOPY

1.1 Sample Preparation and Acquisition Conditions

Cross-section lamellae from the triangular platelet and the rod were prepared on a FEI Scios DualBeam FIB/SEM (Thermo Fisher Scientific). Final polishing at 2 keV minimized surface damage. STEM analysis was performed at 300 kV (probe semi-convergence angle 23.8 mrad) on a probe-corrected Titan Themis 80–300 (Thermo Fisher Scientific) with a beam current of 80 pA to reduce beam damage. Elemental maps were acquired using a Bruker SuperX EDS system.

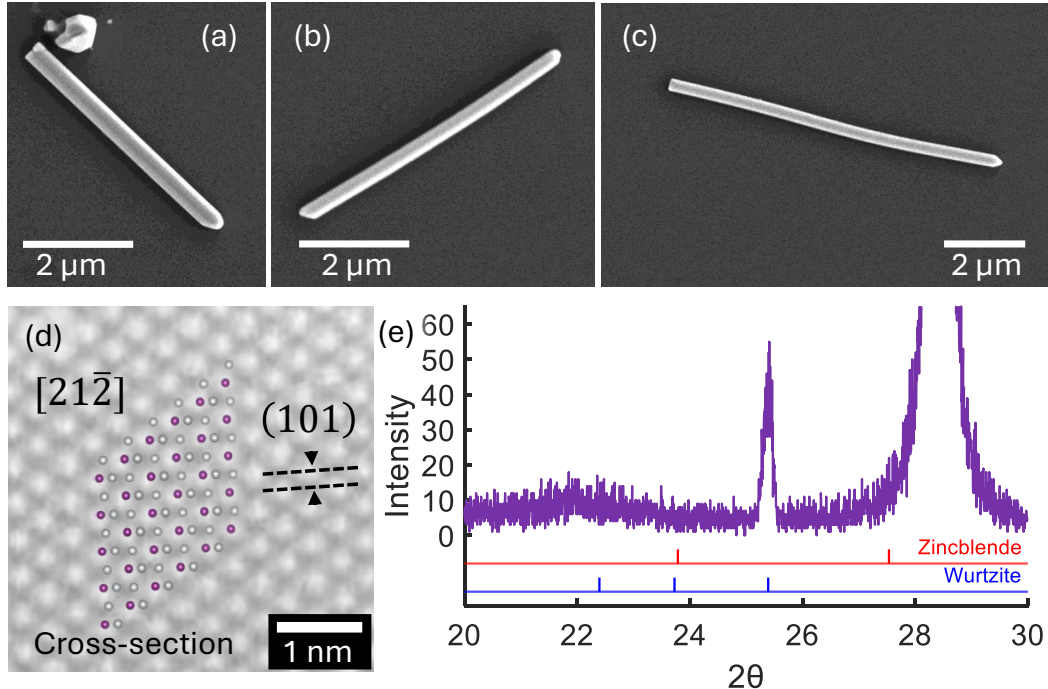


FIG. S1. Characterization of AgI nanorods (β -AgI). (a–c) SEM images of AgI rods grown at 470 °C. (d) HRSTEM image of the rod cross-section acquired along the $[21\bar{2}]$ zone axis; lattice planes indexed to (101) are indicated. (e) X-ray diffraction (XRD) confirming the nanorod growth direction as (101) with a peak at $2\theta = 25.3^\circ$ consistent with the TEM analysis.

1.2 Lattice Indexing and Phase Assignment

Fig S1(d) overlays a crystallographic model on the HRSTEM cross-section acquired along the $[21\bar{2}]$ zone axis, with lattice planes indexed to (101). The assignment is corroborated by the XRD trace in Fig S1(e), which shows a peak at $2\theta = 25.3^\circ$ consistent with β -AgI(101) and the TEM analysis.

2. POLARIZATION-RESOLVED SHG AND 2PPL

We show additional SHG and 2PPL data for AgI nanorods in Fig. S2. A two-fold response appears predominantly in thinner rods. The rod-shaped crystal often showed a sign of degradation before completing the 180° angle rotation, limiting the angle coverage (Fig. S2(a)). The two-fold pattern is consistent with simulation assuming out-of-plane surface of wz-AgI (101).

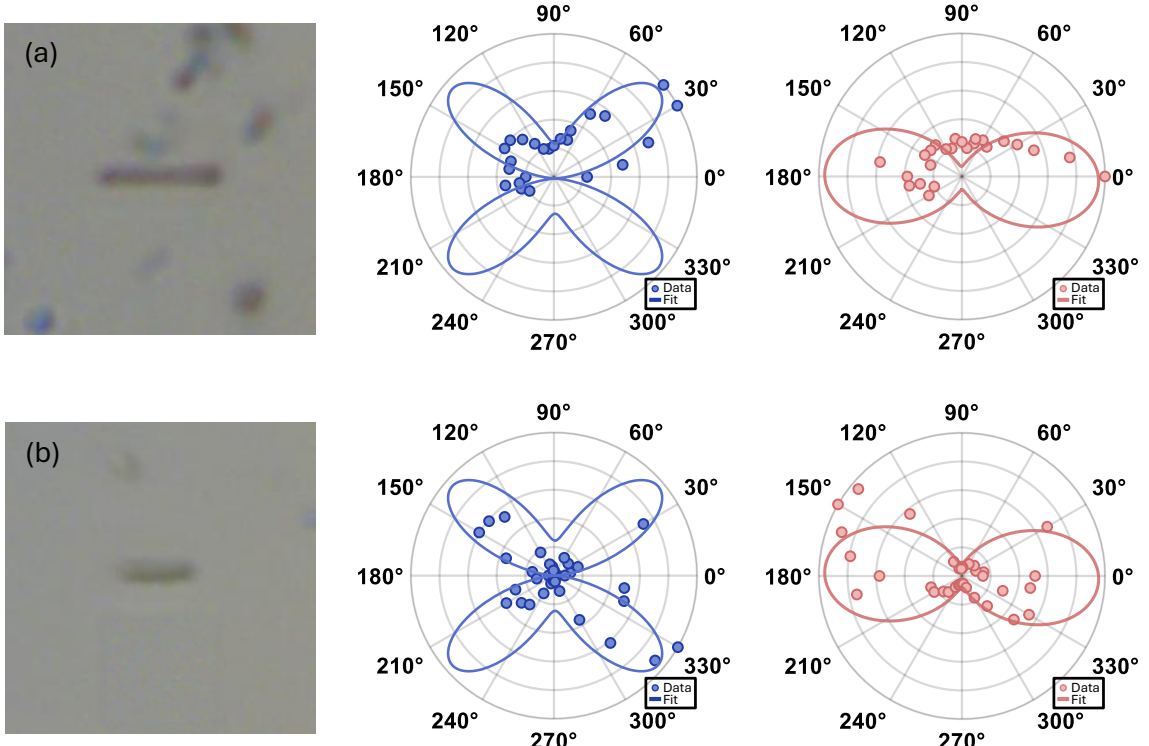


FIG. S2. Polarization-resolved SHG and 2PPL from AgI-rod crystals. For two representative rod-shaped crystals, polar plots of normalized SHG (blue dots) and 2PPL (pink dots) intensity versus in-plane pump-polarization angle δ . SHG exhibits a butterfly shaped two-fold pattern, while 2PPL shows a uniaxial anisotropy with maximum intensity when incident polarization is along the long axis of the rod. All traces are normalized to their own maxima.

3. SHG SIMULATION VALUES

Zincblende

$$\mathbf{d}_{zb} = \begin{bmatrix} 0 & 0 & 0 & d_{14} & 0 & 0 \\ 0 & 0 & 0 & 0 & d_{14} & 0 \\ 0 & 0 & 0 & 0 & 0 & d_{14} \end{bmatrix} \quad \text{with } d_{14} = 1. \quad (S1)$$

Wurtzite

$$\mathbf{d}_{wz} = \begin{bmatrix} 0 & 0 & 0 & 0 & d_{15} & 0 \\ 0 & 0 & 0 & d_{15} & 0 & 0 \\ d_{15} & d_{15} & d_{33} & 0 & 0 & 0 \end{bmatrix} \quad \text{with } d_{15} = 100, d_{33} = 1. \quad (S2)$$

4. 2PPL SIMULATION VALUES

Zincblende

$$\begin{bmatrix} B_{11} & B_{12} & B_{12} & 0 & 0 & 0 \\ B_{12} & B_{11} & B_{12} & 0 & 0 & 0 \\ B_{12} & B_{12} & B_{11} & 0 & 0 & 0 \\ 0 & 0 & 0 & B_{44} & 0 & 0 \\ 0 & 0 & 0 & 0 & B_{44} & 0 \\ 0 & 0 & 0 & 0 & 0 & B_{44} \end{bmatrix}. \quad (\text{S3})$$

Parameter map used in simulations:

$$B_{11} = 1, \quad B_{12} = 0, \quad B_{44} = 0.5 \quad (\text{S4})$$

$$\beta_1^{(\text{zb})} = 1, \quad \beta_2^{(\text{zb})} = 0. \quad (\text{S5})$$

Wurtzite

$$B_{wz} = \begin{bmatrix} B_{11} & B_{12} & B_{13} & 0 & 0 & 0 \\ B_{12} & B_{11} & B_{13} & 0 & 0 & 0 \\ B_{13} & B_{13} & B_{33} & 0 & 0 & 0 \\ 0 & 0 & 0 & B_{44} & 0 & 0 \\ 0 & 0 & 0 & 0 & B_{44} & 0 \\ 0 & 0 & 0 & 0 & 0 & B_{66} \end{bmatrix}. \quad (\text{S6})$$

Parameter map used in simulations:

$$\begin{array}{lll} B_{11} = 0.5 & B_{12} = 0.2 & B_{13} = -0.2 \\ B_{33} = 0.005 & B_{44} = 0.12 & B_{66} = 0.1 \end{array} \quad (\text{S7})$$

$$\beta_1^{(\text{wz})} = 0.005, \quad \beta_2^{(\text{wz})} = 0.08, \quad \beta_3^{(\text{wz})} = 0.5, \quad \beta_4^{(\text{wz})} = -2.2. \quad (\text{S8})$$